Responses of lean swirling spray flames to acoustic pressure and transverse velocity perturbations

Clément Patat, Françoise Baillot, Jean-Bernard Blaisot, Eric Domingues

Symposium on Thermoacoustics in Combustion: Industry meets Academia (SoTiC 2021)
Sept. 6 - Sept. 10, 2021
Munich, Germany
Paper No.: XXX

Responses of lean swirling spray flames to acoustic pressure and transverse velocity perturbations

Clément Patat[1], Françoise Baillot[1], Jean-Bernard Blaisot [1], Éric Domingues[1]

Abstract

Lean liquid-fuel combustion is a promising solution to reduce the polluting emissions of aircraft engines and gas turbines. However, such operating conditions lead more easily to thermo-acoustic instabilities, generally coupled with an azimuthal mode of the cavity, which can be spinning, standing, or a combination of both. With a standing wave, flames are subjected to perturbations in pressure or transverse velocity, depending on their location in the acoustic field. While it is generally admitted that the flame response is mainly dominated by an axial flow oscillation induced by a pressure perturbation, the response of a flame to transverse velocity perturbations is less documented. This is all the more true with spray flames, for which the responses of the gaseous phase and of the liquid phase are different. This paper explores the responses of a linear array of three swirling spray flames at two locations of a standing transverse acoustic field, one characterized by a pressure perturbation and the other by a combination of pressure and transverse velocity perturbations. The Flame Describing Function based on local pressure fluctuations is used to analyze the global flame response. High-speed OH*-imaging is performed in order to evaluate the space-time evolution of the flame response. Spray dynamics is finally examined through PDPA measurements, showing the space-time modulation of the spray, which leads to inhomogeneities in equivalence ratio in the flame zone. The results obtained help to understand the mechanisms leading to the response of swirling spray flames.

Keywords

Combustion instabilities, transverse acoustic forcing, spray flames, swirling flows

Introduction

Gas turbines and aircraft engines are mostly operated with swirling spray flames. To ensure the sustainability of these devices, a significant effort must be produced to find technological solutions that reduce their environmental footprint. A promising solution is to operate in lean combustion, which can lead to a decrease in the emission in soot and nitrogen oxides, and a growth in combustion efficiency. Nevertheless, combustors operating in lean conditions are more susceptible to develop thermo-acoustic instabilities. In annular combustors, these instabilities generally couple with azimuthal modes of the cavity, which can be reproduced experimentally in academic configurations, notably through transverse acoustic forcing. The acoustic field produced inside the combustor may be of various types: standing [1, 2], spinning [3, 4], or a combination between different modes [5]. In the case of standing modes, flames may be subjected to acoustic perturbations in pressure or velocity, depending on their position in the acoustic field. The main effect of pure pressure fluctuations is to induce axial flow fluctuations that are symmetric with respect to the injector axis [6]. These axial fluctuations are generally dominant in the gaseous-flame response. However, when located between a pressure antinode and a velocity antinode, a premixed V-flame was shown to undergo dissymmetric perturbations that might be linked to the crossed contribution of the acoustic pressure and its gradient. Indeed, considering only the pressure gradient cannot explain the intensity of the dissymmetry [7]. Transverse velocity oscillations can also lead to a positive thermo-acoustic coupling via the flame displacement at a velocity antinode [8]. In addition, other types of flame responses can be observed, *e.g.,* high-amplitude instabilities have been shown to induce the extinction of swirling spray flames near the pressure nodal line [2], showing that transverse velocity fluctuations may have a strong effect on the flames. This is consistent with results obtained for a premixed V-flame [7].

Liquid-fuel combustion is also of major interest since most gas turbines are operated with liquid fuels. The presence of a spray introduces supplementary complexity due to the need for the fuel to evaporate and to mix with the air before combustion. Moreover, the presence of two distinct phases implies that their response to an acoustic perturbation is not identical. For an airblast atomizer and in non-reactive conditions, longitudinal acoustic forcing has been shown to generate droplet number density waves [9]. The drop size distribution is modified during the acoustic cycle by the higher sensitivity of small droplets to flow velocity fluctuations [10], but also by the unsteady air momentum.

[1]CORIA-UMR-6614, Normandie Université, CNRS, INSA and Université de Rouen, 76801 Saint-Étienne-du-Rouvray, France

Corresponding author:
Clément Patat, CORIA-UMR-6614, Normandie Université, CNRS, INSA and Université de Rouen, 76801 Saint Etienne du Rouvray, France
Email: clement.patat@coria.fr

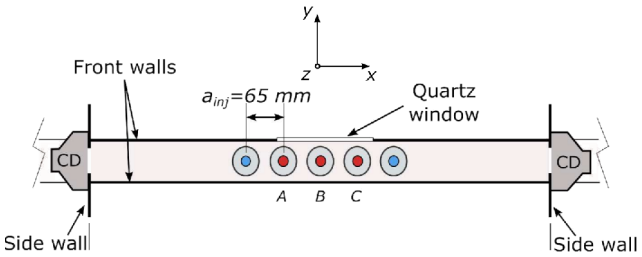

Figure 1. Top view of the acoustic cavity: compression drivers (CD), injectors: red (fuel + air), blue (air)

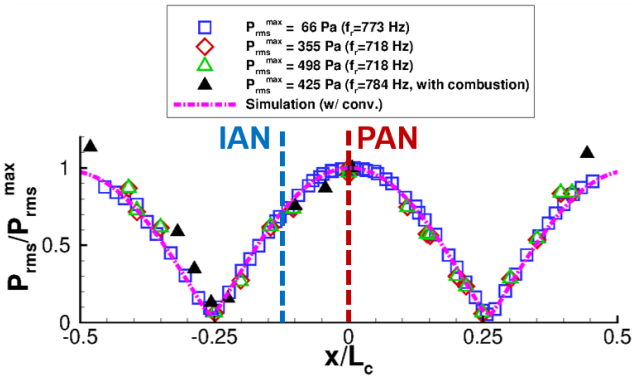

Figure 2. Comparison between the experimental and the simulated acoustic fields inside the cavity, and the two locations of the central flame (injector B) in the present study. PAN/IAN: pressure/intensity antinode.

In particular, for an airblast atomizer, a correlation between drop Sauter diameter D_{32} and air velocity has been found, indicating that D_{32} diminishes as the air velocity increases [11]. Since evaporation is more efficient for small droplets, the evaporation dynamics is modified with the drop size distribution and the air-fuel mixing can be produced more rapidly with small droplets. Thus, these modulations of the spray generates fluctuations of the local equivalence ratio, which is known to be a mechanism for thermo-acoustic instability [12]. In particular, the modification of the evaporation dynamics has been shown to influence self-excited combustion instabilities [13]. Nevertheless, the evaporation rate could be reduced in regions of high droplet number density through droplet clustering, which would therefore act as a damping effect [14]. A more recent numerical work has shown the capability of a liquid-fuel film created on the walls of the injection system to couple with the thermo-acoustic oscillation, leading to self-sustained combustion instability [15]. However, few studies examine spray flame response to both pressure and velocity perturbations in a transverse acoustic field. Consequently, it is of great interest to examine the response of swirling spray flames at various locations of a standing transverse acoustic field. This work aims at understanding how flames located at various positions of a standing transverse acoustic field respond to the acoustic perturbation. It proposes to evaluate the spray flame response via a linear array of three swirling spray flames, while the central flame is placed either at a pressure antinode (PAN) or at an intensity antinode (IAN) of the acoustic field. The latter location combines pressure fluctuations, a pressure gradient and transverse velocity fluctuation, all of them presenting significant amplitudes. A brief description of the experimental setup and post-processing methods is firstly provided. The global flame response is evaluated at both locations, then the space-time flame response is examined through high-speed camera. Finally, an investigation of the spray response is performed.

Materials

Experimental setup: TACC-Spray cavity

The TACC-Spray setup consists in an acoustic cavity in which a linear array of five swirling injectors of exit diameter $D_{exit} = 8$ mm is placed. The acoustic cavity of length $L_c = 880$ mm, height $h_c = 200$ mm and width $e_c = 55$ mm is surmounted by a convergent part of height 60 mm and exit width 10 mm, which avoids outer air to go inside the cavity. Air and liquid n-heptane are supplied to the three central injectors while the two side injectors are fed with air only (see Fig. 1). This configuration helps to stabilize the lateral flames far from the side walls, and therefore helps to keep the central flame in an environment similar to that of the annular combustor MICCA-Spray [2]. Moreover, this setup allows to move the flames inside the cavity, such that it is possible to examine the flame responses at several positions of the forced standing transverse acoustic field corresponding to the 2T1L mode of the cavity (see Fig. 2). Here, the experiments are carried out while the central flame is placed either at a pressure antinode (PAN) or at an intensity antinode (IAN) of the acoustic field. For all measurements, the excitation frequency is tuned to the resonance frequency of the cavity, f_r, which is in the range 715-745 Hz here. The operating point, characterized by a flame power of 5.9 kW and an equivalence ratio $\phi = 0.85$, is set such that the flame response at PAN has a significant amplitude (see [16]).

Diagnostics

Acoustic pressure fluctuations are measured with Brüel & Kjaer Type 4182 microphones at different locations inside the acoustic cavity. In particular, it is measured at the central flame position, which gives the local acoustic pressure P'_{loc}, and at a reference position which is the central PAN, giving P'_{ref}. Thus, when the central flame is located at PAN, $P'_{loc} = P'_{ref}$. The rms acoustic pressure is calculated and reduced by the bulk aerodynamic pressure, which gives a non-dimensional parameter $\Pi_{loc} = P_{loc}^{rms}/\rho^{air}U_{bulk}^2$ showing the balance between acoustics and aerodynamics, where ρ^{air} is the air density and U_{bulk} the bulk velocity at the injector exit, both calculated at 20°C. In the following, the non-dimensional parameter Π_{loc} is taken as indicator of the acoustic forcing level. Its highest attainable value is determined by the acoustic system. Higher values are reached at PAN than at IAN, as shown in Fig. 2. Global flame dynamics is measured with a photomultiplier (PM) Hamamatsu H6779 equipped with an OH*-filter and coupled with a UV-visible lens to focus the flame image on the sensor. High-speed OH*-imaging is performed to investigate the space-time flame dynamics with a Phantom V2012 camera equipped with a Lambert HiCATT 25 intensitifier, a UV-100 mm lens and an UG11 filter. Each series consists of 6,000 images acquired at 20,000 fps. Spray dynamics is examined with a two component-Phase Doppler Particle

Analyzer (PDPA) system, consisting in a source emitting at $\lambda = 488$ nm and $\lambda = 532$ nm coupled with a 250mm-lens and a reception probe equipped with a 500mm-lens and oriented with an angle of 30° with respect to the axis of the source. Measurements are performed at various radial locations $\hat{r} = r/(D_{exit}/2)$ placed on a line passing by the injector axis, which is located at a height $\hat{z} = z/D_{exit} = 0.26$ above the injector exit. Each measurement is performed during 4 s (*i.e.* $\sim$ 3000 acoustic cycles), allowing to collect enough data to ensure statistical convergence.

Post-processing methods

Flame describing function (FDF)

The flame describing function (FDF) framework is used to quantify the global flame response relatively to the acoustic perturbation. Measurements performed with the PM give the OH*-intensity signal I, which can be expressed by the sum of mean ($\overline{I}$) and fluctuating (I') components. The reduced oscillation amplitude $I_{rms}/\overline{I}$, also called flame response, shows the capability of the flame to oscillate around its mean intensity. The local acoustic pressure perturbation P'_{loc} is divided by the aerodynamic pressure based on the velocity, $\rho^{air}U^2_{bulk}$. The pressure fluctuation and the flame intensity oscillation at the excitation frequency f_r, $\breve{I}$ and $\breve{P}$ are calculated in the frequency domain. Therefore, the FDF is written:

$$\mathbb{F}(f_r, \Pi_{loc}) = \frac{\breve{I}/\overline{I}}{\breve{P}_{loc}/\rho^{air}U^2_{bulk}} = G(\Pi_{loc})e^{i\phi(\Pi_{loc})} \quad (1)$$

Since the dimensions of the acoustic cavity are kept identical for all experiments, f_r is similar and the FDF is evaluated at a fixed frequency. As shown by eq. (1), the FDF can also be expressed through a gain G and a phase ϕ. The gain indicates the efficiency of the coupling between acoustics and combustion and the phase expresses the phase delay between the pressure perturbation and the flame response.

Phase-averaging

Acoustically forced signals $s(t)$ present a coherent fluctuation $s^c(t)$ at the forcing frequency in addition to the mean $\overline{s}$ and turbulent fluctuation $s'(t)$ components. Therefore, they can be expressed as follows:

$$s(t) = \overline{s} + s^c(t) + s'(t) \quad (2)$$

Phase-averaging a signal allows to extract its coherent component. However, a sufficient amount of data must be collected in order to cancel the turbulent fluctuation component, whose mean value is assumed to be zero when the quantity of data is high enough. Here, phase-averaging is performed by putting instantaneous data in 20 bins of duration $1/(20f_r) = T/20$, giving the phase-averaged signal $\langle s \rangle(\alpha)$, where α is the phase angle. $\langle s \rangle(\alpha)$ can be expressed as follows for phase angle α_i, where $i \in [1, 20]$ is the bin number:

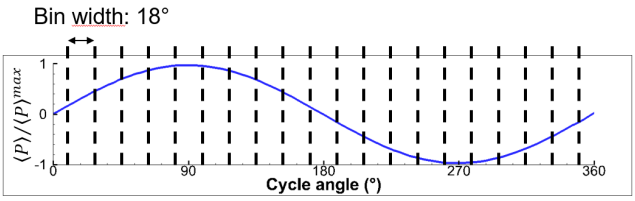

Figure 3. Reconstructed acoustic pressure cycle and its separation in 20 bins for phase-averaging. Bin width: $T/20$.

$$\langle s \rangle(\alpha_i) = \frac{1}{N_{cycles}} \sum_{n=1}^{N_{cycles}} \frac{1}{N^{i,n}_{data}} \sum_{j=1}^{N^{i,n}_{data}} s_j(t_0 + nT) \quad (3)$$

N_{cycles} is the number of acoustic cycles comprised in the measurement and $N^{i,n}_{data}$ the quantity of data into bin i for acoustic cycle n. Bin i is centered around $\alpha_i = 18(i-1)°$. As the bin width is $T/20$, $t_0 + nT$ is actually considered with a tolerance of $\pm T/40$, which explains why multiple data can be acquired in the same bin during the same acoustic cycle. Therefore, a sufficient amount of data can be collected either by increasing the acquisition duration (thus increasing N_{cycles}) or by increasing the acquisition frequency (thus increasing $N^{i,n}_{data}$). Post-synchronization with the acoustic pressure is performed such that the phase-averaged pressure cycle is written in the form:

$$\langle P \rangle(\alpha) = Asin(\omega_r t) \quad (4)$$

where A is the acoustic pressure amplitude and $\omega_r = 2\pi f_r$ is the acoustic angular frequency. The reconstructed acoustic pressure cycle and its separation in 20 bins is presented in Fig. 3. This pressure cycle is taken as a reference in all this work.

High-speed OH*-emission images

Since flames located at IAN experience both acoustic pressure and acoustic velocity perturbations, they are subjected to modulations in axial and transverse velocities. Axial flow modulation is known to induce a heat release rate oscillation [6], while transverse velocity modulation can displace the flames laterally, modifying the spatial repartition of heat release rate. High-speed imaging of the central flame is performed to evaluate the OH*-intensity $I^{cam}_{OH*}(x, z, t)$ integrated along the $\vec{y}$ direction (see Fig. 1). Various post-processings performed on OH* images are described in the following.

Dynamic mode decomposition: Dynamic mode decomposition (DMD) is carried out to extract dynamic modes of the flame OH*-intensity. This algorithm was introduced by Schmid in [17]. For each measurement, a set of 2500 images is taken to perform DMD, corresponding to about 90 acoustic cycles.

Transverse displacement of the flame: Since the transverse velocity modulation can induce a lateral displacement of the flame, the OH*-intensity distribution in the left and right sides of the injector axis can be periodically modified. To evaluate the flame response to the transverse velocity

modulation, the flame is separated in two parts, which are delimited by a vertical line passing by the injector axis. Integration is performed as follows:

$$I_k(t) = \sum_{i=1}^{N_k^{width}} \sum_{j=1}^{N_k^{height}} I_{OH*}^{cam}(x_i, z_j, t) \qquad (5)$$

where k corresponds to the zone in which integration is performed (left part, right part, or the whole flame), N_k^{width} and N_k^{height} are respectively the width and height in pixels of zone k. Phase-averaging is then performed on I_{left}, I_{right} and I_{flame} as indicated by eq. (3), giving the resulting phase-averaged signals $\langle I_{left}\rangle$, $\langle I_{right}\rangle$ and $\langle I_{flame}\rangle$ respectively. If the flame is displaced laterally, the OH*-intensity integrated in one lateral part will be modified due to the displacement induced to acoustics. However, it can also be modified during the acoustic cycle due to effects linked to the axial velocity modulation. These effects can be suppressed by evaluating the reduced signals $\langle I_{left}\rangle^\star = \langle I_{left}\rangle/\langle I_{flame}\rangle$ and $\langle I_{right}\rangle^\star = \langle I_{right}\rangle/\langle I_{flame}\rangle$. These values are finally divided by the mean values without acoustics, $\overline{I_{left}}^{\star,0} = \overline{I_{left}}^{0}/\overline{I_{flame}}^{0}$ and $\overline{I_{right}}^{\star,0} = \overline{I_{right}}^{0}/\overline{I_{flame}}^{0}$.

Induced longitudinal OH-intensity wave:* To extract the longitudinal wave, $I_{OH*}^{cam}(x, z, t)$ is firstly integrated along $\vec{x}$ direction to result in a function of z and t only. This allows to characterize the vertical location of the most reactive regions in the flame and their time evolution. Phase-averaging is then performed by putting the instantaneous OH*-images in 20 bins, each being constructed with around 300 instantaneous images. The resulting OH* signal is then normalized by means of the number of images in a bin, giving the phase-averaged signal $\langle I_{OH*}^{cam}\rangle(z, \alpha)$. This procedure is similar to that described in eq. (3). This allows to define a quantity measuring the coupling between acoustics and combustion:

$$\mathcal{R}(z, \alpha) = \langle P\rangle\langle I_{OH*}^{cam}\rangle(z, \alpha) \qquad (6)$$

which is linked to the Rayleigh criterion. Negative values of $\mathcal{R}$ indicate stable combustion. Positive values of $\mathcal{R}$ indicate that combustion injects energy into the acoustic mode, which is necessary to create an instability. Nevertheless, this is not a sufficient condition, since $\mathcal{R}$ must excess the sum of damping and flux divergence to trigger an instability.

PDPA measurements

Vertical velocity U_z^f and radial velocity U_r^f of the fuel droplets are measured with the PDPA system at various radial locations $\hat{r}$ above the injector exit. Phase-averaging is performed on these data to extract the modulation at f_r (see eq. (3)). As the PDPA system acquires data only when droplets pass through the measurement volume, uneven sampling is performed and $N_{data}^{i,n}(r)$ depends on both i and n, in addition to the radial location. Phase-averaging $N_{data}^{i,n}$ corresponds to measuring the mean droplet count during a time interval of width $T/20$ over all the measurement duration. Therefore, the local phase-averaged droplet count $\langle N\rangle(r, \alpha)$ in bin i is expressed as follows:

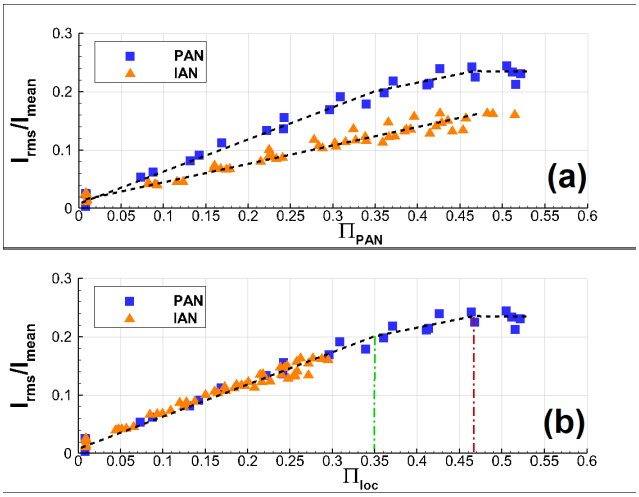

Figure 4. Flame response I_{rms}/I_{mean} for the central flame placed at PAN (blue squares) or IAN (orange triangles). (a) plot vs. acoustic amplitude at PAN Π_{ref}; (b) plot vs. local acoustic amplitude Π_{loc}.

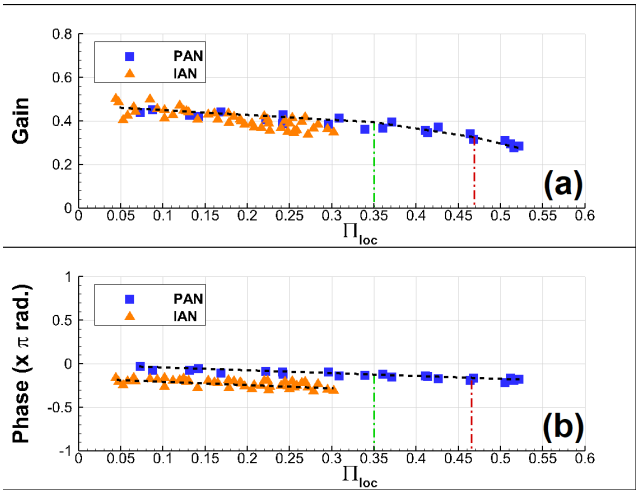

Figure 5. Flame describing function for the central flame placed at PAN (blue squares) or IAN (orange triangles). (a) gain $G(\Pi_{loc})$; (b) phase ϕ_{loc}.

$$\langle N\rangle(r, \alpha_i) = \frac{1}{N_{cycles}} \sum_{n=1}^{N_{cycles}} N_{data}^{i,n}(r) \qquad (7)$$

It gives information about the modulation of the droplet count over the acoustic cycle, but also about the statistical convergence of results. The modulation of the droplet count generates pockets with unequal droplet number density, leading to fluctuations of the local equivalence ratio and droplet clustering. In the following, phase-averaged signals are always indicated between brackets and their dependence on α is omitted for the sake of clarity.

Global flame response to acoustics

The global flame response $I_{rms}/\overline{I}$ measured with PM is shown in Fig. 4 when the central flame is placed either at PAN or at IAN. Plotting the flame response relatively to the reduced acoustic pressure amplitude at PAN, Π_{ref}, allows to show how flames at various locations in the cavity respond

in a same transverse acoustic field. Here, $I_{rms}/\overline{I}$ is higher when the central flame is located at PAN. However, three different regimes are distinguished: a linear growth up to $\Pi_{ref} = 0.35$, followed by a transition zone characterized by a weaker growth of the flame response up to $\Pi_{ref} = 0.47$, and the beginning of a saturation zone above [16]. On the contrary, when the central flame is located at IAN, its response increases linearly up to $\Pi_{ref} = 0.47$. This result may indicate that the flame mainly respond to the local acoustic pressure, whose values at IAN are about 60% of those at PAN. To verify this assumption, the flame response is examined relatively to the local acoustic pressure, Π_{loc}. Here, the comparison between the flame responses at PAN and IAN is only possible in the linear zone, due to the lower value of Π_{loc} reached at IAN. For a same Π_{loc}, $I_{rms}/\overline{I}$ is quite similar at both locations. However, for $\Pi_{loc} > 0.2$, the flame response at IAN is slightly lower than that at PAN. This suggests that when $\Pi_{loc} \leq 0.2$, the flame response at IAN is mainly induced by pressure effects, but other effects may interfere above. It is also interesting to use the FDF framework presented above since it relates the flame response to the acoustic perturbation (see eq. (1)). Here, the acoustic pressure is taken at the flame location since the FDF should be calculated with perturbations effectively experienced by the flame. Results are presented in Fig. 5 at PAN and IAN. The gain is similar at both locations when $\Pi_{loc} < 0.2$, but it slightly higher at PAN than at IAN when $\Pi_{loc} > 0.2$, which confirms the observation made above. The phase is sensitive to a change in the flame location and affected by the increase of acoustic amplitude. Here, this indicates a phase delay between the acoustic pressure and the heat release rate about 0.15π longer at IAN than at PAN. However, its closeness to zero for both locations expresses the in-phase oscillation between the pressure and the heat release rate. This indicates that the flame couples positively with the acoustic perturbation at both locations.

Flame response over space and time

To understand the space-time flame response of the flame, it is worth examining its most energetic dynamic mode of oscillation with the DMD method performed on OH*-images. In Fig. 6, one can see that the flame response at PAN for $\Pi_{loc} = \Pi_{ref} = 0.22$ is symmetric: the longitudinal OH*-intensity wave has a weak amplitude at the flame foot, which increases as the wave propagates downstream, at the same velocity for the left and right sides of the flame. The more intense spots found on the left side of the flame indicates that this side responds a bit more to acoustics. However, a slight dissymmetry in OH*-intensity is also noticed on the unforced flame, indicating that the dissymmetry of the flame response is likely to be induced by effects other than acoustics, *e.g.,* dissymmetry in fuel atomization and therefore in air-fuel mixing. At IAN, the response is estimated for two acoustic amplitudes: i) $\Pi_{loc} = 0.12 \Leftrightarrow \Pi_{ref} = 0.22$, which indicates the response of a flame located in the same acoustic field than the flame at PAN (as shown by the same value of Π_{ref}); ii) $\Pi_{loc} = 0.21 \Leftrightarrow \Pi_{ref} = 0.36$, which gives the response of the flame subjected to the same local pressure perturbation amplitude Π_{loc}. But, the transverse velocity modulation becomes significant for this second acoustic amplitude and may displace the flame laterally. The flame response loses its symmetry for the two acoustic amplitudes examined: the OH*-intensity remains stronger in the left side of the flame (towards PAN), but also propagates faster than that in the right side, resulting in a tilted flame response. This is consistent with results obtained by [7] for non-swirling laminar premixed flames. However, the flame response remains mostly linked to a longitudinal mode induced at the injector exit.

It is interesting to capture the effects of the transverse velocity modulation on the flame, since, as shown by [8] at a velocity antinode, this displacement can feed the thermo-acoustic coupling. Moreover, the flame lateral displacement can induce blow-out [2]. To assess these effects, the proportion of OH*-intensity in the right side of the flame divided by the mean value without acoustics, $\langle I_{right} \rangle^{\star} / \overline{I_{right}}^{\star,0}$, is compared between PAN and IAN. At IAN, the right side is located towards a velocity antinode. Data are shown in Fig. 7(b) for the same Π_{ref}, *i.e.* for the same acoustic field. The associated reconstructed pressure cycle is shown in Fig. 7(a). $\langle I_{right} \rangle^{\star} / \overline{I_{right}}^{\star,0}$ is modulated with an amplitude slightly higher at IAN than at PAN, but in phase opposition. When the pressure is growing, the flame at IAN is displaced towards PAN, which results in a decrease of $\langle I_{right} \rangle^{\star} / \overline{I_{right}}^{\star,0}$. The contrary is observed when the pressure decreases. When the flame is subjected to a same pressure perturbation, *i.e.* a same Π_{loc} (see Fig. 7(c)), the amplitude of $\langle I_{right} \rangle^{\star} / \overline{I_{right}}^{\star,0}$ at IAN is multiplied by 1.4 compared to that for a lower Π_{loc}, but the phase of the modulation is identical. It is clearly shown that the gaseous phase experiences a lateral displacement induced by the transverse velocity modulation. Since the flame is displaced towards regions with a high acoustic pressure amplitude when its heat release rate is high, the instantaneous Rayleigh criterion is increased compared to a non-displaced flame; but the flame is also displaced towards regions where the acoustic amplitude is low when its heat release is low: therefore, the instantaneous Rayleigh criterion is decreased compared to a non-displaced flame. Consequently, when integrated over the acoustic cycle, the Rayleigh criterion should be unmodified by the transverse velocity modulation compared to a non-displaced flame, as soon as the mean flame lateral location does not change.

Therefore, the space-time thermo-acoustic coupling evaluated through the abovementioned quantity $\mathcal{R}$ can be compared between PAN and IAN in Fig. 8. At PAN, a strong coupling is found for 20 mm $< z < 40$ mm. Indeed, as shown by Fig. 6, an OH*-intensity wave propagates downstream and reaches high OH*-levels in this region in phase with the acoustic pressure. For 40 mm $< z < 60$ mm, a negative coupling between acoustics and combustion is observed, arising from the further propagation of the OH*-wave. These two regions are the main contributors to the resulting thermo-acoustic coupling but the positive coupling in the lower regions is much more intense, therefore integrating $\mathcal{R}$ over the whole flame gives a positive value, indicating the potential instability of this operating point. At IAN, the same behaviour is found for the same local acoustic amplitude ($\Pi_{loc} = 0.21$). This indicates that the flame at IAN contributes to sustain the instability through

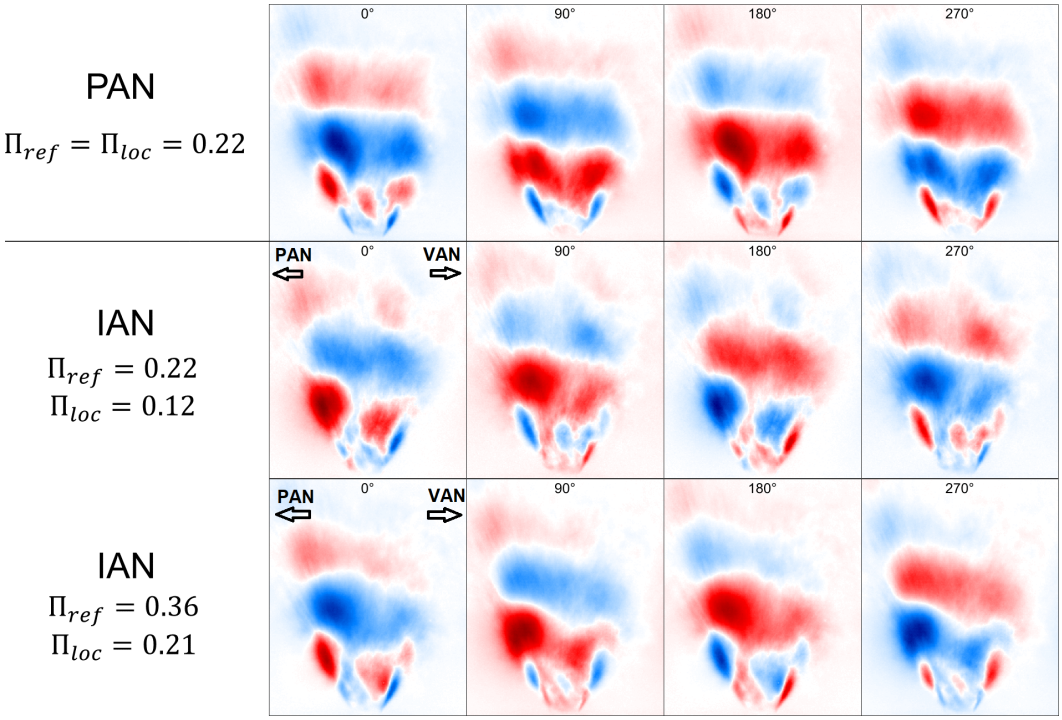

Figure 6. Dynamic mode decomposition of OH*-emission images of the central flame. The location of the flame and the acoustic amplitude are changed accordingly to the indications. The range of the color scale is different for each series.

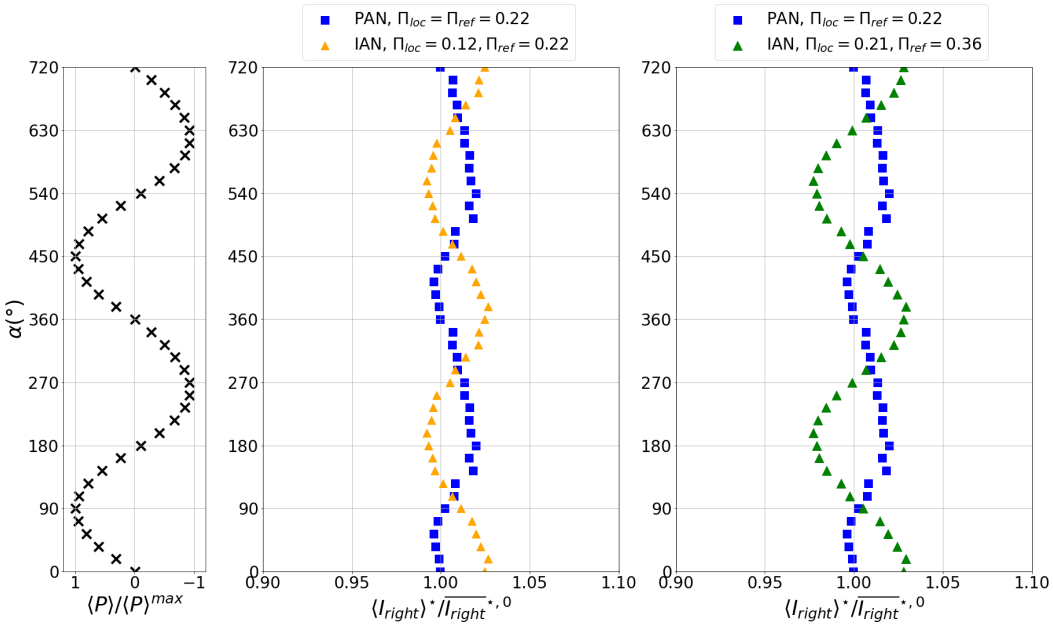

Figure 7. Evolution of the proportion of OH*-intensity in the right side of the injector axis reduced by the mean value without acoustics, $\langle I_{right} \rangle^{\star} / \overline{I_{right}}^{\star,0}$ over a reconstructed acoustic pressure cycle, reproduced twice for the sake of clarity. Left: reconstructed acoustic pressure cycle; middle: $\langle I_{right} \rangle^{\star} / \overline{I_{right}}^{\star,0}$ at PAN (blue squares) and at IAN (orange triangles) for similar values of $\Pi_{ref} = 0.22$; right: $\langle I_{right} \rangle^{\star} / \overline{I_{right}}^{\star,0}$ at PAN (blue squares) and at IAN (green triangles) for similar values of $\Pi_{loc} \simeq 0.22$.

the pressure coupling. However, as shown for $\Pi_{ref} = 0.22$, this contribution is much less intense compared to that of the flame at PAN for the same acoustic field. This suggests that flames located at PAN can drive the instability via the strong pressure coupling at this location, whereas flames at IAN may help in sustaining the instability by injecting energy into the acoustic mode, although at a lower level.

Spray response to acoustics

Earlier work on the same experimental setup showed that at PAN, acoustic pressure modulation induced longitudinal modulations of the count, vertical velocity and size of the droplets resulting in the generation of a droplet number density wave simultaneously to the vertical velocity modulation [16].

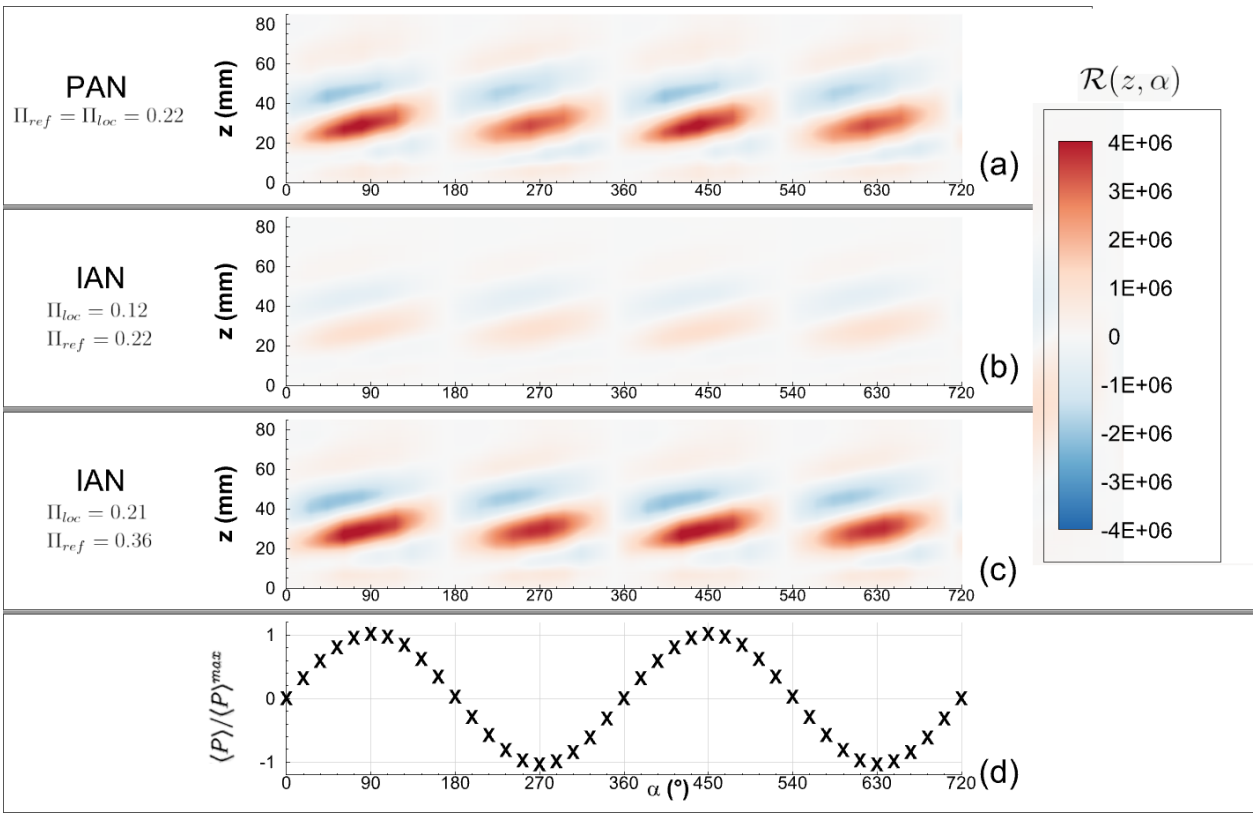

Figure 8. Evolution of the quantity $\mathcal{R}$ measuring the coupling between acoustics and combustion over height during the acoustic cycle reproduced twice. The location of the flame and the acoustic amplitude are changed accordingly to the indications.

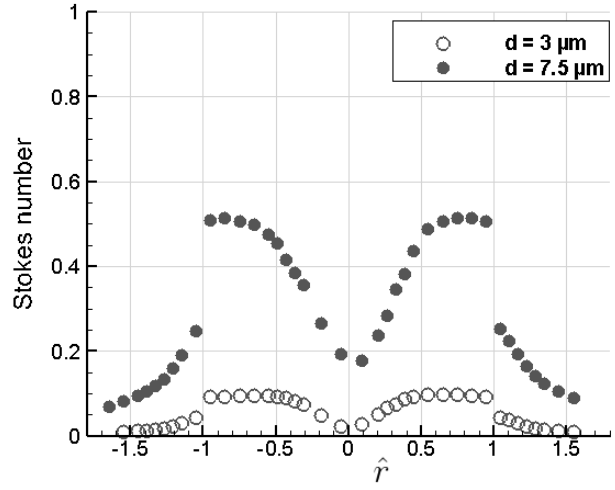

Figure 9. Profiles of Stokes number measured at $\hat{z} = 0.26$ calculated for droplets of diameter 3 µm and 7.5 µm.

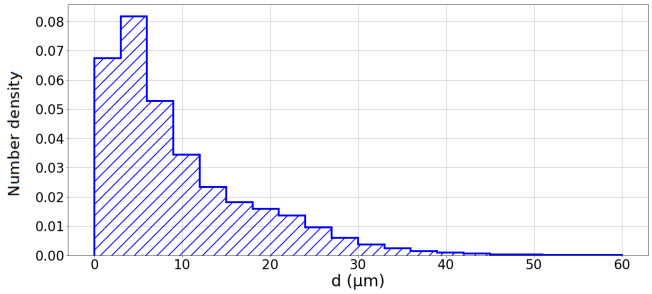

Figure 10. Normalized fuel drop size distribution of the whole spray at $\hat{z} = 0.26$.

Droplet velocity modulation

At a PAN of a transverse acoustic field, vertical velocity modulation is known as an effect of the pressure oscillation. Since the behaviour of the Rayleigh source term is similar at PAN and at IAN, it is interesting to examine the fuel droplet vertical velocity modulation at both locations for a same local acoustic pressure amplitude. Here, the phase-averaged vertical and radial velocities, $\langle U_z^f \rangle$ and $\langle U_r^f \rangle$ respectively, are evaluated for a same Π_{loc} when the central flame is placed at PAN or at IAN. Velocity modulations can be observed more easily by looking at fuel droplets which have a low Stokes number $\mathrm{St} = \frac{\rho_f d^2 U_z^f}{18 \mu^{air} D_{exit}}$, characterizing the ability of droplets to follow the air flow. Here, ρ^f is the fuel density, d the droplet diameter and μ^{air} the air dynamic viscosity, which is calculated at T = 320 K for $|\hat{r}| \leq 1$ and T = 750 K for $|\hat{r}| > 1$. Profiles of the Stokes number calculated for small droplets are shown in Fig. 9. Two profiles are presented: one for droplets of size 3 µm, whose vertical velocity U_z^f is assumed to be the mean velocity of droplets of diameter in the range 1-5 µm; another for droplets of size 7.5 µm, whose vertical velocity is assumed to be the mean velocity of droplets of diameter in the range 5-10 µm. At all radial locations, the Stokes number of the 3 µm droplets is lower than 0.1 while that of the 7.5 µm droplets does not exceed 0.55. Therefore, these droplets should follow air flow fluctuations relatively well. The phase-averaged velocities are thus calculated by means of velocities of droplets satisfying 1 µm $\leq d \leq$ 10 µm, which allows to obtain enough data for statistical convergence. Moreover, they constitute about 65% of the droplet population (see Fig. 10). Fig. 11 shows the modulation amplitude of vertical

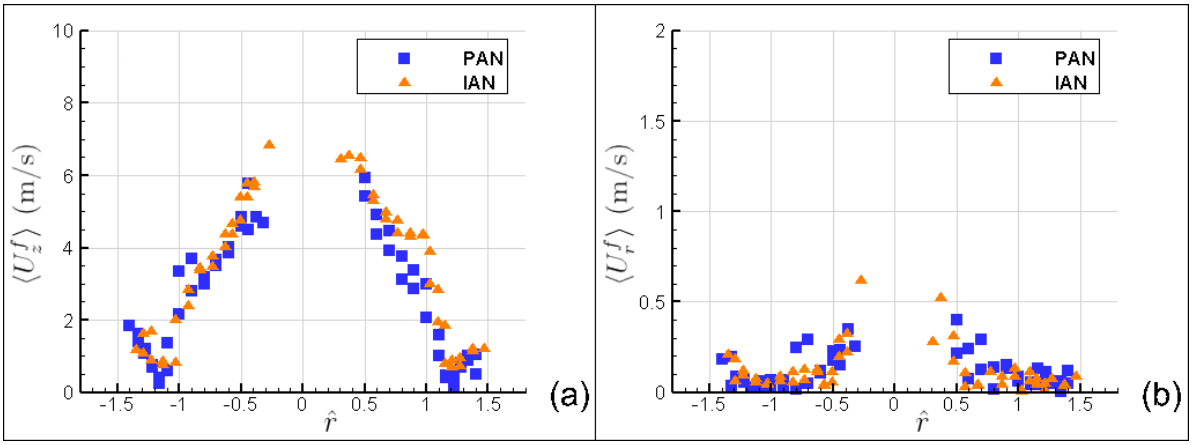

Figure 11. Profiles of the modulation amplitude at $\hat{z} = 0.26$ for $\Pi_{loc} = 0.2$ of: (a) phase-averaged droplet vertical velocity, $\langle U_z^f \rangle$; (b) phase-averaged droplet radial velocity, $\langle U_r^f \rangle$. Velocities are calculated on droplets of diameter comprised between 1 and 10 µm.

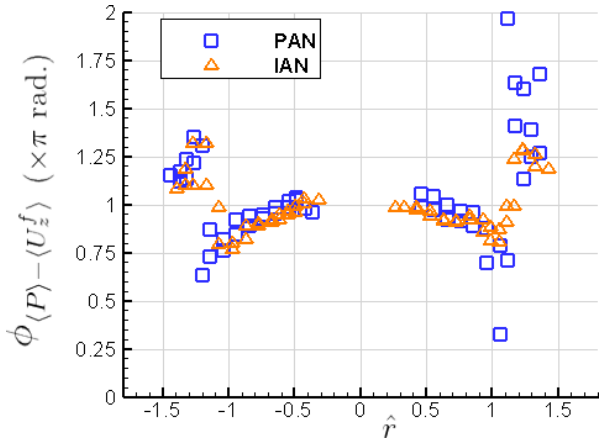

Figure 12. Profile of the phase relationship between $\langle P \rangle$ at the central flame location and $\langle U_z^f \rangle$ at various radial locations $\hat{r}$. $\langle U_z^f \rangle$ is calculated on droplets of diameter comprised between 1 and 10 µm.

and radial velocities, when the central flame is placed at PAN and IAN, for the same $\Pi_{loc} = 0.2$. The modulation amplitude of $\langle U_z^f \rangle$ is symmetric for both PAN and IAN, showing maximum values of 6 m/s for $|\hat{r}| \simeq 0.5$. For lower $|\hat{r}|$, the droplet count is too low to validate the results. The modulation amplitude progressively decreases towards $|\hat{r}| \simeq 1$, then remains weak up to $|\hat{r}| \simeq 1.5$. So, the spray is characterized by an internal region which experiences a strong vertical velocity oscillation, and an external region in which the vertical velocity oscillation is weak. The limit between these two regions can be approximately located at $|\hat{r}| = 1$, which is the vertical projection of the nozzle exit edge. The similarity of the profiles at PAN and IAN indicates that the modulation amplitude of the droplet vertical velocity is insensitive to effects of the pressure gradient noticed in laminar non-swirling premixed flames [7]. As shown in Fig. 12, the phase between the pressure perturbation at the flame location and the vertical velocity modulation is also similar at PAN and IAN. In the internal region of the spray, $\langle U_z^f \rangle$ oscillates in phase opposition with the pressure. In the external region, it deviates from phase opposition, but the weak modulation amplitude may increase uncertainty about the results. The modulation amplitude of $\langle U_r^f \rangle$ (see Fig. 11 (b)) at IAN is as weak as at PAN, and the low levels may be attributed to noise. These results indicate that the liquid phase only responds to the pressure perturbation at the injector exit, similarly at PAN and at IAN; neither effects of the transverse velocity nor of the pressure gradient are measured at IAN in the vicinity of the nozzle exit.

Generation of droplet spatial number density wave

The phase-averaged droplet count $\langle N \rangle$ is evaluated at various radial locations via the method described in eq. (7). Indeed, the oscillation in droplet population may generate a modulation of the equivalence ratio, leading to a heat release rate oscillation. A high droplet count may also generate clustering effects, thus reducing evaporation. Fig. 13 shows results for $\langle N \rangle$ at PAN and IAN for $\Pi_{loc} = 0.2$. For both locations in the acoustic field, the response to the acoustic perturbation is similar at the nozzle exit, supporting the assumption that the spray response mostly depends on the pressure perturbation. A densely populated region is found for $|\hat{r}| > 1$ when the acoustic pressure is positive. This high number of droplets is injected with a low mean vertical velocity of about 15-20 m/s. It is followed, when the acoustic pressure is negative, by a decrease of $\langle N \rangle(r, \alpha)$, which is approximately divided by a factor 2. For $0.5 < |\hat{r}| < 1$, a high number of droplets is injected when the acoustic pressure is negative, but their mean vertical velocity is in the range 35-43 m/s. Simultaneously, droplets are measured for $|\hat{r}| < 0.5$, which is an unpopulated region without acoustics. But, when the acoustic pressure is positive, this region empties and a weak spatial density is even found up to $|\hat{r}| = 0.6$. At the same time, droplets are less rapid. Therefore, at the nozzle exit, the internal region ($\hat{r} \leq 1$) is characterized by the injection of many fast droplets, followed by less slower droplets, while the external region ($\hat{r} > 1$) is characterized by an oscillating droplet count, but droplets remain relatively slow during all the acoustic cycle. This complex injection pattern results in a space-time modification of the droplet number density, leading to fluctuations of the local equivalence ratio after evaporation, which may however be diminished if dense droplet clusters are present [14]. The strongest flame response found for 20

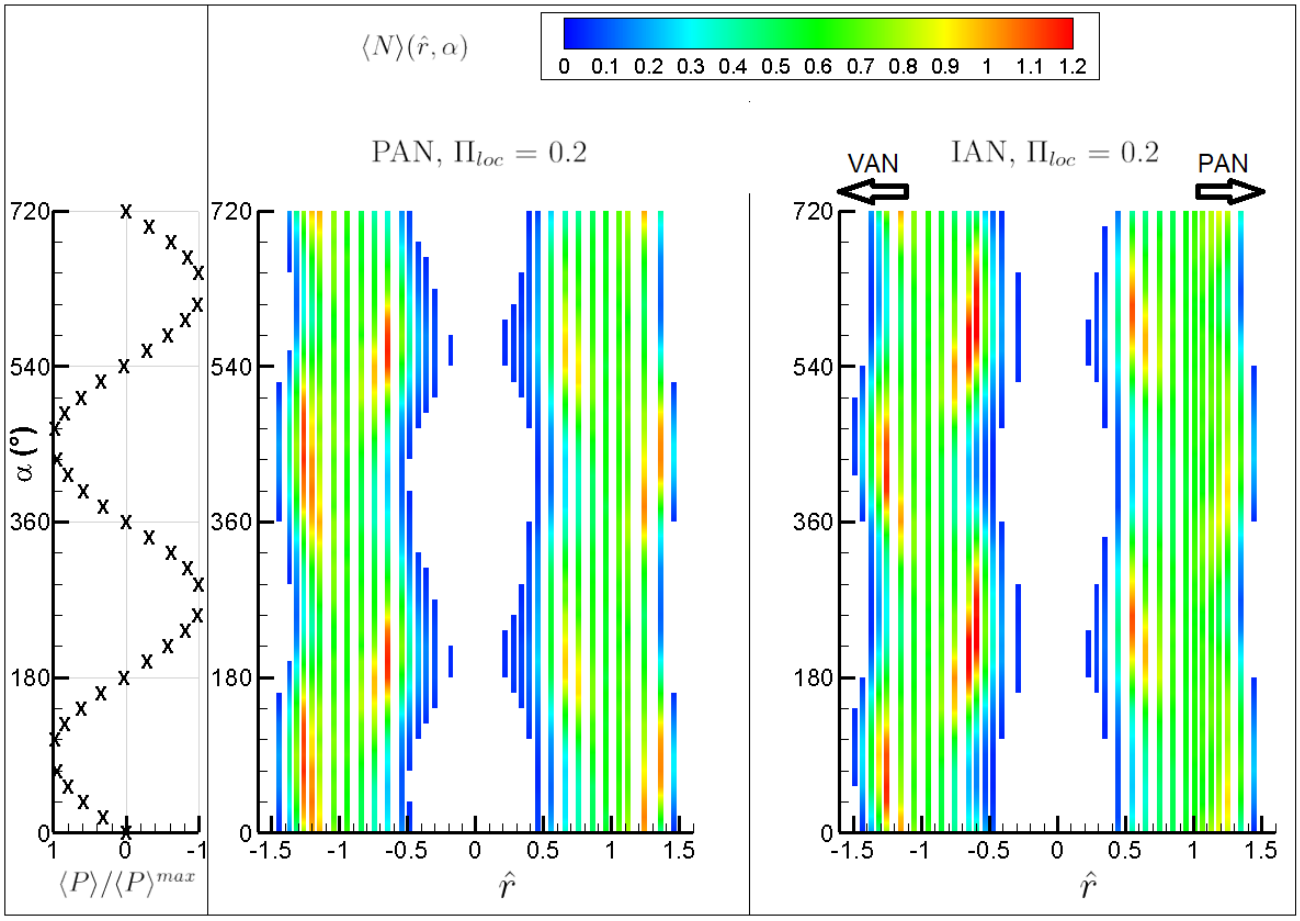

Figure 13. Evolution of the droplet count $\langle N \rangle(r, \alpha)$ over a reconstructed acoustic pressure cycle, reproduced twice for the sake of clarity. Left: Reconstructed acoustic pressure cycle; middle: $\langle N \rangle(r, \alpha)$ at PAN for $\Pi_{loc} = 0.2$, $f_r = 715$ Hz; right: $\langle N \rangle(r, \alpha)$ at IAN for $\Pi_{loc} = 0.2$; $f_r = 729$ Hz. White zones indicate a droplet count too low for validation.

mm $< z <$ 40 mm indicates that this region is particularly sensitive to the modulations induced by acoustics. Thus, understanding the interaction between the droplet number density waves generated in the internal and external regions and the flame response requires to examine the resulting equivalence ratio fluctuations and their transport to the flame front.

Conclusion

A linear array of three swirling spray flames is submitted to transverse acoustic perturbations. The central flame is placed either at a pressure antinode (PAN) of the standing acoustic field, or at an intensity antinode (IAN), which combines perturbations in pressure, transverse velocity and pressure gradient. The Flame Describing Function, calculated with respect to the local pressure, has a similar gain but a slightly different phase at both locations. At PAN, the flame response is symmetric while at IAN, a dissymmetry is observed, which may be linked to the periodic lateral displacement of the flame induced by the transverse velocity modulation. Space-time flame dynamics shows that at both locations, the flame response is dominated by the middle part of the flame, where a periodic OH*-intensity wave fluctuates in phase with the pressure oscillation, thus feeding the thermo-acoustic coupling. It is shown that the flame at PAN is the main contributor to thermo-acoustic coupling, but the flame at IAN also injects energy in the acoustic mode. Analysis of the spray shows the weak sensitivity of fuel droplets to the transverse velocity modulation at the injector exit. However, a complex injection pattern induced by the pressure perturbation generates droplet number density waves at the injector exit, inducing local equivalence ratio fluctuations at higher locations. Further understanding requires to examine the resulting equivalence ratio fluctuations and their transport to the flame zone.

Acknowledgements

This work was supported by the French National Research Agency (ANR) through the project FASMIC ANR-16-CE22-0013, Région Normandie and French Ministry of Higher Education and Research. The authors wish to thank RENADIAG for the technical support provided to this research.

References

[1] O'Connor J, Worth N and Dawson J. Flame and flow dynamics of a self-excited, standing wave circumferential instability in a model annular gas

turbine combustor. *Proceedings of the ASME Turbo Expo* 2013; (GT2013-95897).

[2] Vignat G, Durox D, Renaud A et al. High amplitude combustion instabilities in an annular combustor inducing pressure field deformation and flame blow off. *Journal of Engineering for Gas Turbines and Power* 2019; 142(1): 011016.

[3] Mazur M, Nygård H, Dawson J et al. Characteristics of self-excited spinning azimuthal modes in an annular combustor with turbulent premixed bluff-body flames. *Proceedings of the Combustion Institute* 2019; 37: 5129–5136.

[4] Bourgouin JF, Durox D, Moeck J et al. Characterization and modeling of a spinning thermoacoustic instability in an annular combustor equipped with multiple matrix injectors. *Journal of Engineering for Gas Turbines and Power* 2015; 137: 021503–1.

[5] Bourgouin JF, Durox D, Moeck J et al. A new pattern of instability observed in an annular combustor: The slanted mode. *Proceedings of the Combustion Institute* 2015; 35(3): 3237–3244.

[6] O'Connor J, Acharya V and Lieuwen T. Transverse combustion instabilities: Acoustic, fluid mechanic, and flame processes. *Progress in Energy and Combustion Science* 2015; 49: 1–39.

[7] Lespinasse F, Baillot F and Boushaki T. Responses of v-flames placed in an hf transverse acoustic field from a velocity to pressure antinode. *Comptes Rendus Mécanique* 2013; 341: 110–120.

[8] Schwing J and Sattelmayer T. High-frequency instabilities in cylindrical flame tubes: feedback mechanism and damping. *Proceedings of ASME Turbo Expo* 2013; : GT2013–94064.

[9] Gajan P, Strzelecki A, Platet B et al. Investigation of spray behavior downstream of an aeroengine injector with acosutic excitation. *Journal of Propulsion and Power* 2007; 23(2): 390–397.

[10] Giuliani F, Gajan P, Diers O et al. Influence of pulsed entries on a spray generated by an airblast injection device: an experimental analysis on combustion instability processes in aeroengines. *Proceedings of the Combustion Institute* 2002; 29: 91–98.

[11] Eckstein J, Freitag E, Hirsch C et al. Experimental study on the role of entropy waves in low-frequency oscillations in a rql combustor. *Journal of Engineering for Gas Turbines and Power* 2006; 128: 264–270.

[12] Huang Y and Yang V. Dynamics and stability of lean-premixed swirl-stabilized combustion. *Progress in Energy and Combustion Science* 2009; 35: 293–364.

[13] de la Cruz Garcia M, Mastorakos E and Dowling A. Investigations on the self-excited oscillations in a kerosene spray flame. *Combustion and Flame* 2009; 156: 374–384.

[14] Réveillon J and Demoulin F. Evaporating droplets in turbulent reacting flows. *Proceedings of the Combustion Institute* 2007; 31: 2319–2326.

[15] Lo Schiavo E, Laera D, Riber E et al. Effects of liquid fuel/wall interaction on thermoacoustic instabilities in swirling spray flames. *Combustion and Flame* 2020; 219: 86–101.

[16] Baillot F, Patat C, Cáceres M et al. Saturation phenomenon of swirling spray flames at pressure antinodes of a transverse acoustic field. *Proceedings of the Combustion Institute* 2020; 38(4): 5987–5995.

[17] Schmid P. Dynamic mode decomposition of numerical and experimental data. *Journal of Fluid Mechanics* 2010; 656: 5–28.